Large Eddy Simulation of Soot Formation in a Model Gas Turbine Combustor

Heeseok Koo,
Postdoctorate Appointee, Member of ASME
Department of Aerospace Engineering
University of Michigan
Ann Arbor, Michigan 48109
Email: heeseokkoo@gmail.com

Malik Hassanaly [*],
Graduate Student, Member of ASME
Department of Aerospace Engineering
University of Michigan
Ann Arbor, Michigan 48109
Email: malik.hassanaly@gmail.com

Venkat Raman,
Associate Professor, Member of ASME
Department of Aerospace Engineering
University of Michigan
Ann Arbor, Michigan 48109
Email: ramanvr@umich.edu

Michael E. Mueller
Assistant Professor, Member of ASME
Department of Mechanical
and Aerospace Engineering
Princeton University
Princeton, New Jersey 08544
Email: muellerm@princeton.edu

Klaus Peter Geigle
Senior Researcher, Member of ASME
German Aerospace Center (DLR)
Institution of Combustion Technology
Pfaffenwaldring 38-40, D-70569
Stuttgart, Germany
Email: klauspeter.geigle@dlr.de

ABSTRACT

The computational modeling of soot in aircraft engines is a formidable challenge, not only due to the multi-scale interactions with the turbulent combustion process but the equally complex physical and chemical processes that drive the conversion of gas-phase fuel molecules into solid-phase particles. In particular, soot formation is highly sensitive to the gas-phase composition and temporal fluctuations in a turbulent background flow. In this work, a large eddy simulation (LES) framework is used to study soot formation in a model aircraft combustor with swirl-based fuel and air injection. Two different configurations are simulated: one with and one without secondary oxidation jets. Specific attention is paid to the LES numerical implementation such that the discrete solver minimizes the dissipation of kinetic energy. Simulation of the model combustor shows that the LES approach captures the two recirculation zones necessary for flame stabilization very accurately. Further, the model reasonably predicts the temperature profiles inside the combustor. The model also captures variation in soot volume fraction with global equivalence ratio. The structure of the soot field suggests that when secondary oxidation jets are present, the inner recirculation region becomes fuel lean and soot generation is completely suppressed. Further, the soot field is highly intermittent suggesting that a very restrictive set of gas phase conditions promote soot generation.

Nomenclature

A Soot surface area
C Progress variable
D Diffusivity

[*]Corresponding author

k_{resol} Resolved turbulent kinetic energy
k_{resid} Residual turbulent kinetic energy
$M_{x,y}$ Soot moment of x, y orders in volume and surface area
M Pope's criterion
S^M Moment source
t Time
T Temperature
U_x, U_y Horizontal/tangential and axial velocity components
u_j Velocity vector
V Soot volume
x, y Horizontal and axial directions
x_j Spatial coordinate
Z Mixture fraction
ν Viscosity
ρ Density

1 Introduction

Modeling and simulation of soot remains a formidable challenge in spite of the significant progress that has been made in the numerical modeling of turbulent combustion [1]. This complexity arises from the myriad of physical and chemical processes that transform fuel-bound carbon to carbonaceous particles, with the entire particle evolution process spanning many orders of length and time scales. Nevertheless, laminar flame studies and related fundamental modeling of kinetic rates have vastly improved the predictive capabilities of soot models in such flows. However, the performance of such models in turbulent flames has not been robust [1, 2], with good predictions in certain flames [3] and several orders of magnitude difference in other cases [4, 5]. Since almost all of these studies have been conducted in canonical flames such as jet diffusion and bluff-body stabilized flames, it is unclear whether soot model performance can be extrapolated to more complex aircraft combustor flows. Mueller and Pitsch [6] have simulated soot formation in a gas turbine combustor, but those studies lacked rigorous experimental quantification. The focus of this work is to evaluate soot models in realistic geometries, where high-fidelity experimental data is available.

The most significant advance in the field of numerical simulations is the advent of large eddy simulation (LES), which has transformed the predictive landscape for gas phase simulations in complex geometries. In LES, large scale features of the flow are directly resolved on a computational grid, while small-scale physics, including the processes that control soot formation, are modeled. In flows where large scale mixing is dominant, LES is able to predict key statistics such as velocity or scalar fields rather accurately [7–9]. On the other hand, when small-scale physics such as droplet-based fuel release or extinction/ignition are important, LES results are highly sensitive to the models used. In this sense, LES is roughly as accurate as the more conventional Reynolds-averaged Navier Stokes (RANS) approach. Soot introduces another level of complexity. Although the initial gas-phase conversion of fuel molecules to soot precursors occurs at the small-scales, soot evolution itself is a slow process and happens over many integral length scales. Consequently, soot formation is a unique process that couples small-scale generation to slower large scale flow evolution. Consequently, both the LES mixing prediction and the small-scale physical/chemical processes that evolve soot particles become important.

In developing numerical models, it is important to recognize the extreme sensitivity of soot formation to gas-phase composition. In other words, small changes in the gas phase temperature or species mass fractions can dramatically increase or suppress soot formation. This places a higher importance on numerical errors introduced by the solution to the LES governing equations. It is well-known that the use of Taylors-series based finite-difference or finite volume methods introduce errors in the numerical solution of LES equations [10–13]. In particular, numerical errors scale with wavenumber implying that they are highest near the filter scale. This contaminates the solution at the smallest resolved scale, which in turn affects the evaluation of sub-filter models. Hence, mitigating this source of error is important for capturing soot generation in flames.

A useful metric of numerical accuracy in such flows is discrete kinetic energy conservation. In all low-Mach number flows, LES uses a fractional time-stepping procedure that recognizes the decoupling between kinetic energy and thermal energy. Consequently, the kinetic energy of the flow is not directly solved for. However, it has been shown that numerical algorithms that preserve kinetic energy discretely, without solving explicitly for this quantity, are found to be more accurate in capturing the turbulent flow structures [14]. In simple geometries, staggered mesh formulations have been used to enforce this discrete conservation. However, in complex collocated unstructured grids, such energy conservation is difficult to preserve.

With this discussion, the focus of the current work is two-fold. First, we implement a numerically accurate LES solver that adequately captures the complex flow structure inside a model aircraft combustor. An open source computational tool (OpenFOAM [15]) is used as the codebase for this LES solver development. This experimental configuration was studied using high-fidelity diagnostic tools at DLR [16]. Second, detailed soot models are used to predict particle generation and

evolution inside this combustor. Two different configurations, with and without secondary air injection, are studied. In particular, the effect of flow configuration on the intermittent soot formation in such combustors is studied. As will be shown, in relation to prior work by the authors [17], these results present a marked change in predictive capabilities, primarily due to the improved numerical accuracy of the LES solver.

2 LES Modeling of Soot and Numerical Implementation

The LES implementation here is designed to reproduce soot formation in complex geometries. The application in this work is an ethylene-fueled model gas turbine combustor [16].

2.1 Gas-phase and Soot Models

The LES governing equations are obtained by filtering the corresponding conservation equations for mass, momentum, and species concentrations. For the sake of brevity, these equations are not repeated and the readers are referred to other articles [8, 9]. The evolution of soot equations and the associated rates are based on the model proposed by Mueller [18–20]. Some details are provided here in order to aid discussion of results. Essentially, the number density function of soot ($N(\zeta;\mathbf{x},t)$) is described in terms of volume and surface area ($\zeta = \{V,A\}$), and transport equations for a set of moments of this number density function is used to obtain local soot distribution. The moments are expressed as

$$M_{x,y} = \int V^x A^y N d\zeta \tag{1}$$

where x,y are the orders of the moment in volume and surface area, respectively. The transport equation for the moments obtained from the population balance equation using the above definition of moments in Eqn. (1) can be written as:

$$\frac{\partial M_{x,y}}{\partial t} + \frac{\partial u_j M_{x,y}}{\partial x_j} = \frac{\partial}{\partial x_j}\left(0.55\frac{\nu}{T}\frac{\partial T}{\partial x_j}M_{x,y}\right) + S^M_{x,y}(\zeta,\xi) \tag{2}$$

where $S^M_{x,y}$ represents the moment source terms accounting for nucleation, growth, and oxidation of soot particles, and ξ is a vector of thermochemical composition variables. A nucleation model based on dimerization of polycyclic aromatic hydrocarbon (PAH) [21] is used in this study, and other models that account for the source terms follow Mueller *et al.* [19]. The first term on the right hand side is the thermophoresis of soot particles [20], which is replaced by a conventional diffusion flux using mass diffusivity in this study. Since only a finite number of moments are solved for, the moment source terms are unclosed. Closure is obtained with the hybrid method of moments (HMOM) [19].

Soot inception depends on accurate modeling of not only the fuel oxidation but also the formation of soot precursors such as PAH. Therefore, a combustion model is needed that can account for this detailed chemistry. In this work, the radiation flamelet/progress variable (RFPV) model for sooting flames developed by Mueller and Pitsch [5] is used. This model accounts for gas-phase radiation using an optically thin assumption. The thermochemical composition vector ξ is parameterized using three variables, namely, mixture fraction Z, a reaction progress variable C, and a radiation heat loss parameter H. Transport equations for the variables representing the thermochemical composition vector are written as follows:

$$\frac{\partial \rho\kappa}{\partial t} + \frac{\partial \rho u_j \kappa}{\partial x_j} = \frac{\partial}{\partial x_j}\left(\rho D\frac{\partial \kappa}{\partial x_j}\right) + \rho\mathbf{S}(\kappa) \tag{3}$$

where $\kappa = [Z,C,H,Y_{PAH}]$ and $\mathbf{S}(\kappa) = [S_Z,S_C,S_H,S_{PAH}]$. Note here that PAH removal due to soot formation results in a source for the nominally conserved scalar Z. The flamelet equations [22] are solved, and the solutions are stored in a table for subsequent look-up of the source terms. Variance of Z is calculated using Z gradients and the filter size with a local equilibrium assumption [23]. The local equilibrium is assumed not being compromised from the range of Z source magnitudes considered in this study. In addition to the steady flamelet solutions, the RFPV approach includes unsteady flamelet solutions for parameterizing with respect to H to reflect heat exchange through radiations from both gas and soot phases. Further details of the RFPV approach can obtained from Mueller and Pitsch [5]. In the LES formulation, these equations are filtered, leading to unclosed terms. Models for such terms are provided elsewhere [5, 20].

2.2 Low Dissipation Implementation in OpenFOAM

In this section, we focus on the kinetic energy conservation properties of the LES solver. As discussed in the introduction, preserving or minimizing discrete kinetic energy loss is essential for the robust solution of a turbulent flow field. The LES

implementation is based on a low-Mach number formulation [24–26], which uses pressure to enforce the filtered continuity equation. In this sense, density changes directly affect the pressure field, leading to dilatation of the velocity field applied as a correction to an intermediate velocity solution.

In the OpenFOAM code base, a new solver was created to handle variable-density, flamelet-based LES computations [27]. The energy-conservation strategy is based on the scheme proposed by Morinishi [28]. This scheme reduces to the approach of Ham and Iaccarino [14] in the limit of constant density flows. The OpenFOAM solver uses a collocated variable placement, where fluxes are obtained by interpolation to cell faces. This interpolation as well as the required pressure gradient at the cell faces are computed using a second-order linear interpolation. For a uniform mesh, the linear interpolation becomes a mid-point interpolation scheme that minimizes an energy loss [29].

The mid-point interpolation is also applied in the time direction, where the momentum transport equations are evolved from time n to $n+1$, while the individual terms in the equation are evaluated at time $n+1/2$ obtained using interpolation method. This implicit formulation is crucial for the conservation of kinetic energy. In other words, ensuring convergence of the time discretization is important to minimizing discrete energy loss. In the OpenFOAM solver, this is ensured using PISO (pressure-implicit second order) iterations [30]. It has been shown that two PISO iterations are sufficient to achieve second order convergence in time [30]. This strategy is targeted toward statistically stationary flow problems since PISO procedure introduces a stronger coupling and allows a larger time step. For a more general tool, fractional time-step procedure can be utilized [31]. With the goal of capturing the flame location accurately, a stronger coupling between the scalar and density fields is introduced. The velocity at time $n+1$ is used in the scalar transport equation rather than the velocity at time $n+\frac{1}{2}$. Second, the time-rate of change of density, which is needed to update pressure, uses a second-order Crank-Nicholson scheme rather than a first-order Euler scheme.

To demonstrate the energy conservation properties of this solver, verification studies using canonical flow configurations were considered (similar to that in [32]). A Taylor-Green vortex with no density change was computed on orthogonal and skewed meshes. Figure 1 shows the solution on these two grids at the same computed time. It can be seen that the solver preserves the vortical structures even in a skewed mesh representation, which is important for application to complex geometries. Figure 2 shows the decay of kinetic energy for this test case. Not only the implemented approach is unaffected by mesh skewness, it shows comparable amounts of energy loss to Ham and Iaccarino's formulation [14]. As mentioned earlier, exact conservation cannot be achieved in a collocated mesh scheme. Instead, energy dissipation is minimized using the procedure described above. The truncation error of kinetic energy evolution is $O(\Delta x^2 \Delta t)$, implying that a smaller time step ensures better conservation properties as well. The extension to variable density is based on the scheme of Morinishi [28], which enforces kinetic energy conservation through a strictly skew-symmetric form of the convection terms but is not predicated on the simultaneous conservation of mass. This is different from the conventional low-Mach number approaches [33] in ensuring that no additional error is introduced in the kinetic energy conservation. Note that compared to icoFOAM, one of the conventional OpenFOAM solvers, the implemented approach reduces kinetic energy loss by 16% and 94% for the orthogonal and skewed meshes, respectively. For the orthogonal case, the difference mostly rely on the semi-implicit coupling of timesteps. For the skewed case, the kinetic energy conservative spatial discretization schemes become effective and explain the larger discrepancy. This improved LES solver for unstructured grids is then used for the simulations described below.

3 DLR Swirl Combustor

3.1 Simulation Configuration and Numerical Details

The experimental configuration [16] replicates an aircraft engine with the fuel being introduced between swirled oxidizer jets. Further, a set of injection ports located on the side walls is used to replicate secondary air injection in rich-quench-lean type aircraft engines. The ethylene-based combustor operates at a global equivalence ratio of roughly 1.5, which, for this fuel, is located very close to the maximum soot forming region. The use of the secondary injection ports reduces the global equivalence ratio to 1.15. Three cases are studied: a non-reacting flow case, and a case with and one without secondary injection.

Figure 3 shows the computational mesh used in this work, and is similar to the mesh used in [17]. The number of computational volumes was 5-7 million based on the cases studied, with the secondary injection grid requiring refined grid near the injection ports. The main combustor itself is geometrically simple, but the inflow ducts that pass through the swirler require detailed calculations. It was found that the flow profile at the exit of the inflow nozzles into the combustor directly affects the size of the recirculation zone and the stability of the combustion processes. For this reason, several grids were used to understand the impact of numerical discretization on the spatial evolution of the swirling flow. The computational mesh used here was found to provide the best performance with minimal grid resolution.

The mesh quality is further assessed and plotted in Fig. 3 using Pope's criterion [34, 35]. Here, M is defined as the ratio

between the residual (sub-filter) kinetic energy and the total kinetic energy.

$$M = \frac{k_{resid}}{k_{resol} + k_{resid}}, \tag{4}$$

where the residual kinetic energy is obtained using the scaling relations provided in [34]. While some portions of the inflow region is not adequately resolved, the mesh quality is acceptable in the primary flame region. More importantly, further refinement did not affect the statistics of the gas-phase flow field. Hence, it is argued that this mesh is adequate for the purposes intended in this work.

The combustion chamber is 110 mm in length, and spans a cross-section of 85 mm $\times$ 85 mm. The inflow air swirls through the complex passages in the injector section, and mixes with fuel in the chamber. The fuel is injected through a round-shape slit with a size of 0.347 mm between air streams that pass through two different swirlers. The air mass flow rate incoming from the bottom swirlers is 3.2267 g/s, and the fuel stream mass flow rate is 0.3283 g/s. Secondary oxidizer streams are injected with a mass flow rate of 0.9667 g/s through four 3.5 mm diameter additional ducts at two-thirds the height of the chamber. Reactants are finally exhausted through a circular tube at the top to atmospheric pressure.

The detailed chemical mechanism of Blanquart et al. [36] extended by Narayanaswamy et al. [37] is used to construct the flamelet library. Some of the parameters required to calculate soot moment sources are also stored in the library. Locations of the progress variable and several coefficients of soot evolution sources are plotted in mixture fraction (Z) and progress variable (C) space in Fig. 4. Soot production through dimer occurs at a fuel rich condition, and so does the growth through surface reaction. Meanwhile, soot oxidation is maximized in fuel lean regions. Note here that stoichiometric condition is at $Z = 0.064$ for an ethylene-air combustion. The LES computations are performed on 512 cores, with each simulation taking roughly 200 hours. With a maximum allowed CFL of 1.5, the time-step size is approximately 1.5 μs. Statistics were collected over ten flow-through times, defined based on the inflow bulk jet velocity and the chamber height. Soot statistics presented in the results section are averaged in the four homogeneous directions from the centerline normal to the side walls.

3.2 Non-reacting Flow Case

To ensure that the LES solver captures the general flow structure reasonably well, a non-reacting flow simulation was conducted. The corresponding experimental conditions are provided in [38]. The air mass flow rate is 4.68 g/s at the bottom of the swirlers, with air being injected through the fuel injection slit with a mass flow rate of 0.362 g/s. The upstream temperature of the fluid is maintained at 330K [39]. The experimental data includes statistical averages of axial and tangential velocity measurements.

Figure 5 shows mean axial and tangential velocity contours. The algorithmic modifications made in this work led to tangential swirl angles that were consistent with experimental data. In particular, the injection angle was higher than corresponding angle in our earlier work [17]. Similarly, the axial velocities provide the high velocity region near the walls that is essential for separating the inner recirculation region (located near the center of the combustor) and the outer recirculation zone (between the high-velocity region and the wall). This structure is also important for predicting the flame stabilization process (discussed below). Direct comparison with PIV data is shown in Figure 6, where line data extracted from the 2D images shown in Fig. 5 are compared with PIV data. It is seen that the simulations predict very well the flow structure found in experiments. In particular, the sharp peaks in velocity profiles (both components) are well captured, providing high confidence in the accuracy of the solver.

4 Reacting Flow Cases

The reacting flow cases comprise of two simulations, with and without secondary air injection. Below, gas phase data is analyzed first followed by the soot data.

4.1 Gas Phase Results

Figure 7 shows the axial velocity comparison for the two cases (with and without secondary injection). As seen, the simulations are able to predict the flow structure reasonably well, including the injection velocity angle from the swirl nozzles. Similar agreement was found for the tangential component (not shown here). It should be noted that the inner recirculation region has expanded due to the heat release from combustion. For the case with secondary injection, the simulations predict a weaker inner recirculation region, but the overall structure is roughly the same as in the case without secondary injection.

Figure 8 shows the time-averaged mixture fraction and temperature fields. Stoichiometric mixture fraction for this fuel is roughly $Z_{st} = 0.064$. Without secondary air injection, the mixture fraction values in the inner recirculation zone are much higher than this value, promoting the formation of soot. In the case with secondary injection, the soot-favorable mixture

fraction is confined to the narrow shear layers between the inner and outer recirculation zones. The temperature profiles show that the bulk of the combustor exhibits near-uniform temperature in the case without secondary injection. But with the secondary jets, the temperature profile exhibits "cool" spots where the side jets interact.

The time-averaged mean and RMS temperature profiles are compared to experiments in Fig. 9. It is seen that the simulations predict the drop in temperature near the centerline due to the secondary air jets. However, the centerline temperature profile shows higher peak near the burner surface, indicating that the inner recirculation zone anchors the flame. However, in the experiments, the temperature drops significantly close to the nozzle exit, implying that the flame location is lower than in the experiment due to the stronger vortex near the bottom wall. The RMS profiles are predicted at levels close to the experiment, but with the reduced mean temperature profiles, this actually implies a higher level of turbulent fluctuations than in the experiments. Regardless, considering experimental uncertainties as well as the non-density weighted experimental data, the agreement is reasonably accurate.

4.2 Soot Volume Fraction Results

Figures 10 and 11 show instantaneous soot volume fraction contours at several different time instances. Soot exhibits highly intermittent behavior, with peak soot values observed only sporadically. These sporadically-formed soot structures in Figs. 10 and 11 are qualitatively similar to the small scale soot filaments reported in the experiment [16]. Note that the inner recirculation region has the right gas phase conditions to generate soot almost continuously, and thus provides a baseline soot generation region. However, the majority of the soot is generated in regions close to the wall where the inner and outer recirculation zones merge. Here, low strain rates combined with low velocities and high temperatures promote soot growth. When secondary jets are present, soot production is significantly reduced. This is due to two reasons. First, the mixture fraction in the inner recirculation region falls below the critical value needed to generate soot. At the same time, presence of excess oxygen quickly oxidizes soot at these high temperatures.

Comparison of soot volume fraction statistics (Figs. 12 and 13) show that the simulations are able to predict the sooting tendencies of both cases reasonably accurately. Compared to canonical jet flame calculations [2, 4], the level of agreement is very good in this geometry. In particular, the ability to predict RMS soot distribution is very promising. As expected, soot volume fraction decreases substantially when the secondary jets are present. This is a combined effect of a lower equivalence ratio and the jet momentum of the secondary air flows. In both cases, the RMS soot volume fraction is comparable in magnitude to the mean, further emphasizing the role of intermittent soot generation. In the case with secondary injection, there is an asymmetry in soot profiles due to the placement of the secondary jets on the side walls, which is also captured well by the experiments. In the case with no secondary injection, the inner recirculation zone appears to be the main source of soot generation. It is unclear if such a large variation in the flame structure is present in practical gas turbines as well.

5 Conclusion

A model gas turbine combustor was studied using LES with advanced numerical and computational models. An open source computational tool was modified to enhance the numerical accuracy of the LES solution. A minimally dissipative numerical scheme was used to improve the flow field predictions. Comparisons with experimental data showed that this modification improved the ability to capture the swirling flow. In particular, the strong shear layers associated with the swirl based injection of fuel was captured very well. Similarly, the simulations were able to predict the temperature profiles reasonably well, including the dip in gas phase temperature near the center of the combustor due to the interactions of the air jets from the secondary injection ports. Such sensitivity to boundary conditions provided confidence in the ability of the model to predict soot formation.

The soot volume fraction in reacting cases was also predicted reasonably well, with the main features of the two cases captured. The presence of secondary injection decreased the overall equivalence ratio inside the combustor, which led to unfavorable conditions for soot formation. It was found that such a reduction in equivalence ratio altered the structure of the inner recirculation zone, and fully eliminated soot formation in this region. In both cases, soot formation was found to be intermittent with large variances of the soot volume fraction. It is important to note that the quantitative discrepancies are more difficult to decipher given the complexities of the flow. From the simulations, it can be concluded that since soot intermittency drives the overall volume fraction statistics, capturing not only the one-point one-time statistics but also the time correlations are important. Consequently, experimental measurements that can provide such statistics should be sought.

Acknowledgements

This work was supported by SERDP grant WP-2151 with Dr. Robin Nissan as the Program Manager. The authors also gratefully acknowledge the generous allocation of computing time by the Texas Advanced Computing Center and NASA High-End Computing (HEC) Program through the NASA Advanced Supercomputing (NAS) Division at Ames Research Center.

References

[1] Raman, V., and Fox, R. O., 2016. "Modeling of fine-particle formation in turbulent flames". *Annual Review of Fluid Mechanics,* ***48***, pp. 159–190.

[2] Donde, P., Raman, V., Mueller, M. E., and Pitsch, H., 2013. "LES/PDF based modeling of soot-turbulence interactions in turbulent flames". *Proceedings of the Combustion Institute,* ***34***, pp. 1183–1192.

[3] Mueller, M. E., Chan, Q. N., Qamar, N. H., Dally, B. B., Pitsch, H., Alwahabi, Z. T., and Nathan, G. J., 2013. "Experimental and computational study of soot evolution in a turbulent nonpremixed bluff body ethylene flame". *Combustion and Flame,* ***160***, pp. 1298–1309.

[4] The second International Sooting Flame Workshop (ISF2), http://www.adelaide.edu.au/cet/isfworkshop/2014/, accessed on 17.02.2016.

[5] Mueller, M. E., and Pitsch, H., 2012. "LES models for sooting turbulent nonpremixed flames". *Combustion and Flame,* ***159***, pp. 2166–2180.

[6] Mueller, M. E., and Pitsch, H., 2013. "Large eddy simulation of soot evolution in an aircraft combustor". *Physics of fluids,* ***25***, 110812.

[7] Raman, V., Pitsch, H., and Fox, R. O., 2005. "A consistent hybrid LES-FDF scheme for the simulation of turbulent reactive flows". *Combustion and Flame,* ***143***(1-2), pp. 56–78.

[8] Kempf, A., Lindstedt, R. P., and Janicka, J., 2006. "Large-eddy simulation of bluff-body stabilized nonpremixed flame". *Combustion and Flame,* ***144***(1-2), pp. 170–189.

[9] Raman, V., and Pitsch, H., 2005. "Large-eddy simulation of bluff-body stabilized non-premixed flame using a recursive-refinement procedure". *Combustion and Flame,* ***142***(4), pp. 329–347.

[10] Ghosal, S., 1996. "An analysis of numerical errors in large-eddy simulations of turbulence". *Journal of Computational Physics,* ***125***(1), Apr., pp. 187–206.

[11] Chow, F., and Moin, P., 2003. "A further study of numerical errors in large-eddy simulations". *Journal of Computational Physics,* ***184***(2), pp. 366–380.

[12] Kaul, C. M., Raman, V., Balarac, G., and Pitsch, H., 2009. Effect of numerical errors on sub-filter scalar variance models. *Physics of Fluids,* ***21***(5), 055102.

[13] Kaul, C. M., and Raman, V., 2011. "A posteriori analysis of numerical errors in subfilter scalar variance modeling for large eddy simulation". *Physics of Fluids,* ***23***(3), 035102.

[14] Ham, F., and Iaccarino, G., 2004. "Energy conservation in collocated disretization schemes on unstructured meshes". In CTR Annual Research Briefs.

[15] The open source cfd toolbox. OpenCFD Inc. http://www.openfoam.com/.

[16] Geigle, K. P., Zerbs, J., Köhler, M., Stöhr, M., and Meier, W., 2011. "Experimental analysis of soot formation and oxidation in a gas turbine model combustor using laser diagnostics". *Journal of Engineering for Gas Turbines and Power,* ***133***, 121503.

[17] Koo, H., Raman, V., Mueller, M. E., and Geigle, K. P., 2015. "Large-eddy simulation of a turbulent sooting flame in a swirling combustor". In 53rd AIAA Aerospace Science Meeting, no. AIAA 2015-0167.

[18] Mueller, M. E., 2012. "Large eddy simulation of soot evolution in turbulent reacting flows". PhD thesis, Stanford University.

[19] Mueller, M. E., Blanquart, G., and Pitsch, H., 2009. "Hybrid method of moments for modeling soot formation and growth". *Combustion and Flame,* ***156***, pp. 1143–1155.

[20] Mueller, M. E., and Pitsch, H., 2011. "Large eddy simulation subfilter modeling of soot-turbulence interactions". *Physics of fluids,* ***23***, 115104.

[21] Blanquart, G., and Pitsch, H., 2009. *Combustion Generated Fine Carbonaceous Particles*. Karlsruhe University Press.

[22] Pierce, C. D., and Moin, P., 2004. "Progress-variable approach for large-eddy simulation of non-premixed turbulent combustion". *Journal of Fluid Mechanics,* ***504***, pp. 73–97.

[23] Germano, M., Piomelli, U., Moin, P., and Cabot, W. H., 1991. "A dynamic subgrid-scale eddy viscosity model". *Physics of Fluids,* ***7***, pp. 1760–1765.

[24] Kim, J., and Moin, P., 1985. "Application of a fractional-step method to incompressible Navier-Stokes equations". *Journal of Computational Physics,* ***59***(2), pp. 308–323.

[25] Akselvoll, K., and Moin, P., 1996. "Large eddy simulation of turbulent confined coannular jets". *Journal of Fluid Mechanics,* ***315***, pp. 387–411.

[26] Pierce, C. D., 2001. "Progress-variable approach for large-eddy simulation of turbulence combustion". PhD thesis, Stanford University.

[27] Lietz, C., Tang, Y., Koo, H., Hassanaly, M., and Raman, V., 2015. "Large eddy simulation of a high-pressure multi-jet combustor using flamelet modeling". In 10th OpenFOAM Workshop.

[28] Morinishi, Y., 2010. "Skew-symmetric form of convective terms and fully conservative finite difference schemes for variable density low-mach number flows". *Journal of Computational Physics,* ***229***, pp. 276–300.

[29] Felten, F. N., and Lund, T. S., 2006. "Kinetic energy conservation issues associated with the collocated mesh scheme

for incompressible flow". *Journal of Computational Physics,* ***215***, pp. 465–484.
[30] Issa, R. I., 1985. "Solution of the implicitly discretised fluid flow equations by operator-splitting". *Journal of Computational Physics,* ***62***, pp. 40–65.
[31] Kravchenko, A. G., and Moin, P., 1997. "On the effect of numerical errors in large eddy simulations of turbulent flows". *Journal of Computational Physics,* ***131***, pp. 310–322.
[32] Mahesh, K., Constantinescu, G., and Moin, P., 2004. "A numerical method for large-eddy simulation in complex geometries". *Journal of Computational Physics,* ***197***, pp. 215–240.
[33] Nicoud, F., 2000. "Conservative high-order finite-difference schemes for low-mach number flows". *Journal of Computational Physics,* ***158***, pp. 71–97.
[34] Pope, S. B., 2000. *Turbulent Flows*, Chapter 13. 3-13. 4, Cambridge University Press.
[35] Pope, S. B., 2004. "Ten questions concerning the large-eddy simulation of turbulent flows". *New Journal of Physics,* ***6***(35).
[36] Blanquart, G., Pepiot-Desjardins, P., and Pitsch, H., 2009. "Chemical mechanism for high temperature combustion of engine relevant fuels with emphasis on soot precursors". *Combustion and Flame,* ***156***(3), pp. 588–607.
[37] Narayanaswamy, K., Blanquart, G., and Pitsch, H., 2010. "A consistent chemical mechanism for oxidation of substituted aromatic species". *Combustion and Flame,* ***157***, pp. 1879–1898.
[38] Widenhorn, A., Noll, B., Stöhr, M., and Aigner, M., 2008. "Numerical characterization of the non-reacting flow in a swirled gasturbine model combustor". *High Performance Computing in Science and Engineering*, pp. 431–444.
[39] Widenhorn, A., Noll, B., and Aigner, M., 2010. "Numerical characterization of a gas turbine model combustor". *High Performance Computing in Science and Engineering*, pp. 179–195.

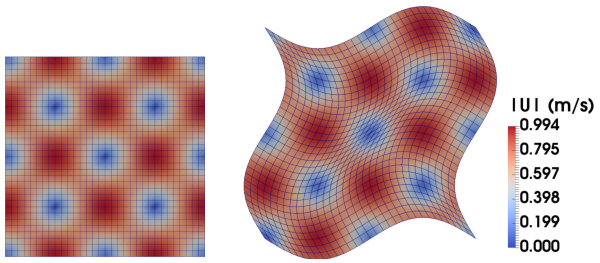

Fig. 1. Velocity magnitude contours after 1 second for orthogonal and skewed meshes.

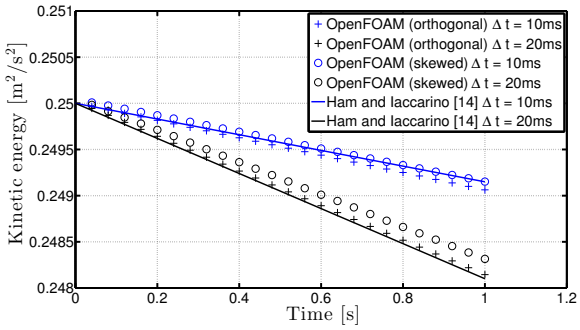

Fig. 2. Temporal kinetic energy decay between different numerical approaches for orthogonal and skewed meshes, for two different timestep sizes. Ham and Iaccarino results (solid lines, [14]) correspond to both orthogonal and skewed mesh cases.

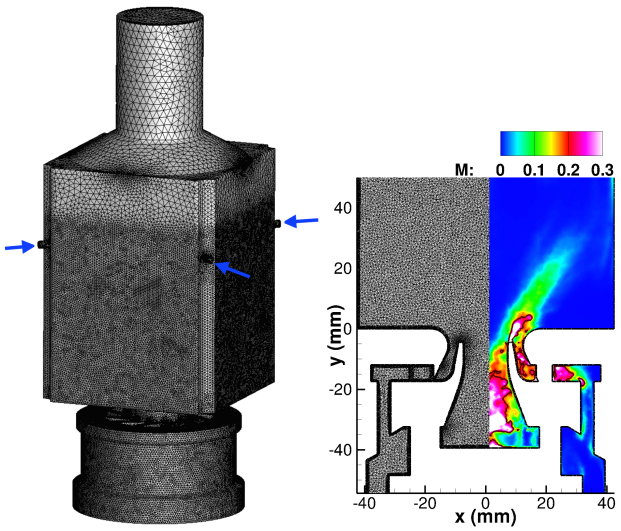

Fig. 3. (a) Full three-dimensional grid with secondary inlets marked. (b) The center plane mesh with the Pope's criterion. M=0.2 along the solid lines.

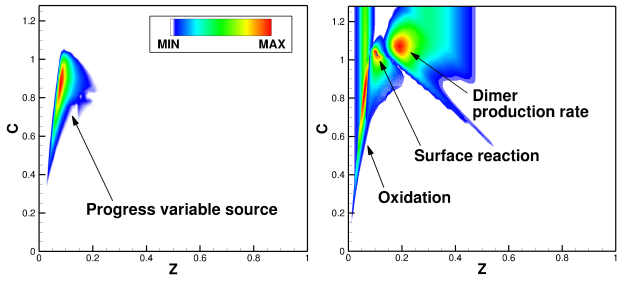

Fig. 4. Flamelet solutions showing (a) progress variable source term, S(C) in Eqn. (3), and (b) key soot chemistry source terms.

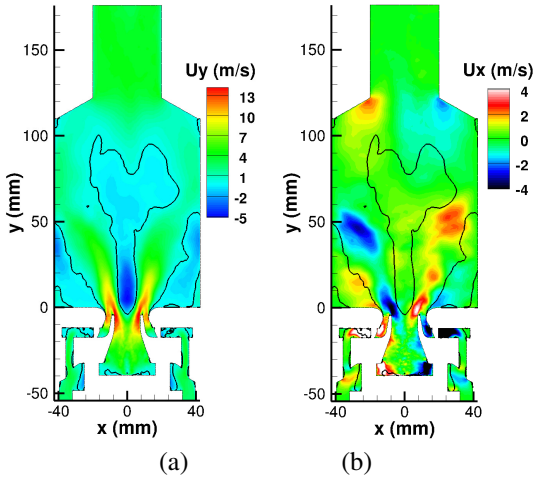

Fig. 5. Mean (a) axial (Uy) and (b) tangential (Ux) velocity contours from LES. Axial velocity is zero along the solid lines.

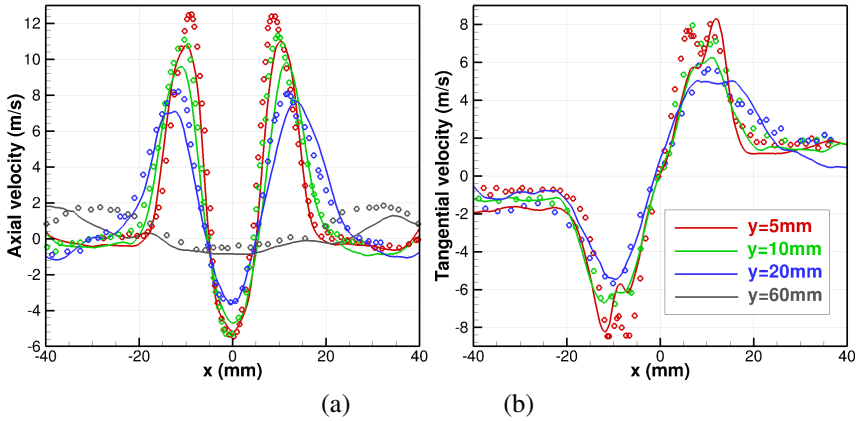

Fig. 6. Mean (a) axial and (b) tangential velocities from LES (solid lines) compared to experimental data (circles) at different axial locations.

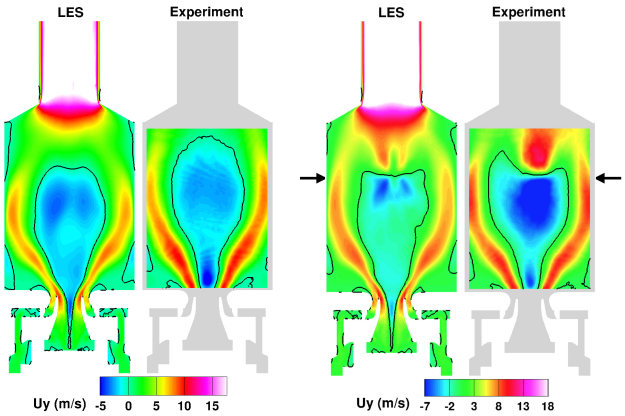

(a) No secondary flow (b) With secondary flow

Fig. 7. Mean axial velocities for the case with and without secondary injections, compared to the experimental PIV data [16]. Axial velocity is zero along the solid lines.

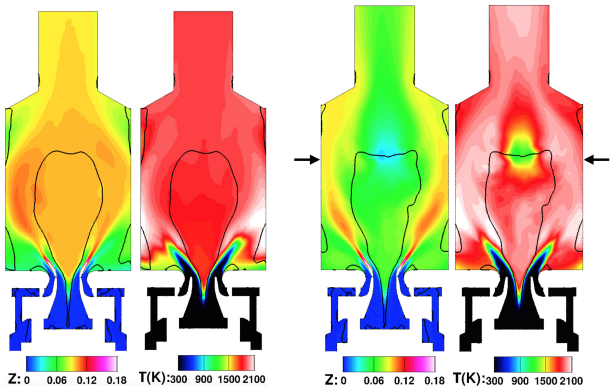

(a) No secondary flow (b) With secondary flow

Fig. 8. Mean mixture fraction and temperature fields.

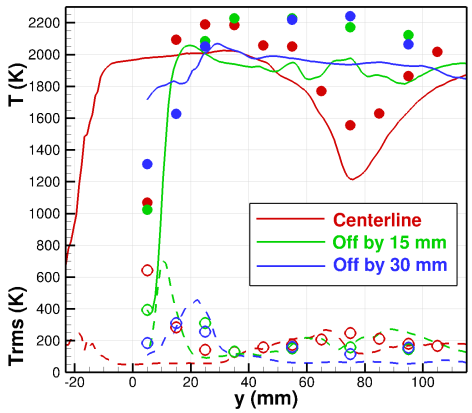

Fig. 9. Mean and rms temperature profiles along the centerline and two off-center axial lines for the case with secondary air injection. Solid lines and filled circles are mean temperature profiles while dashes and empty circles are rms values.

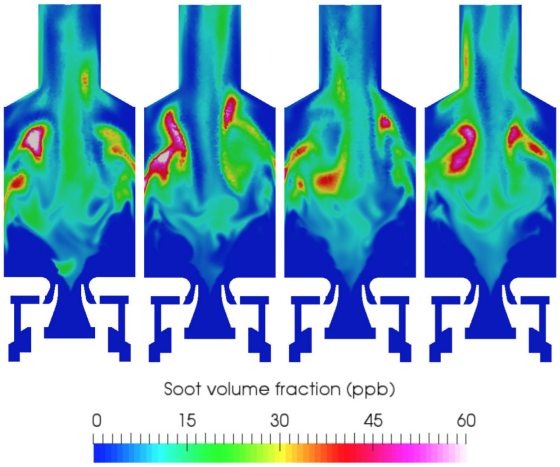

Fig. 10. Instantaneous soot volume fraction snapshots at the center plane every 8 milliseconds for the case without secondary injection.

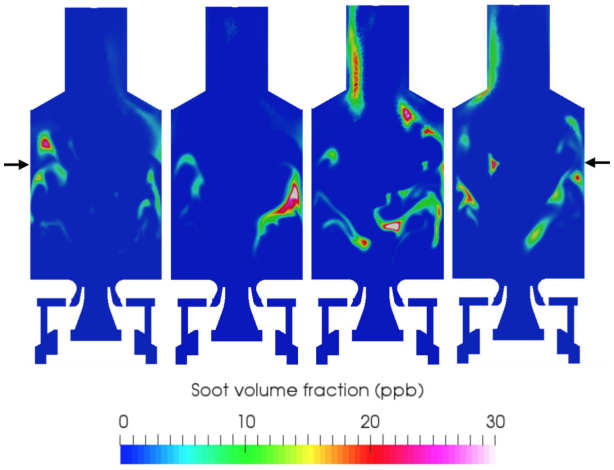

Fig. 11. Instantaneous soot volume fraction snapshots at the center plane every 8 milliseconds for the case with the secondary injection.

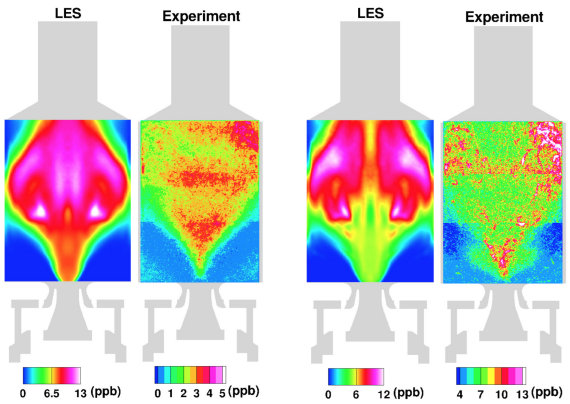

(a) Mean soot volume fraction (b) RMS volume fraction

Fig. 12. Soot volume fraction statistics for the case without secondary air injection compared to the experiment.

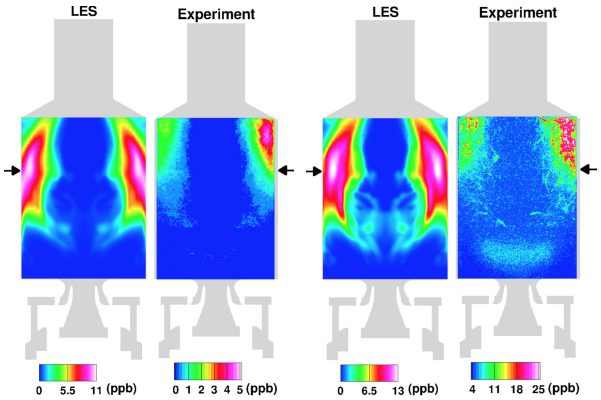

(a) Mean soot volume fraction (b) RMS volume fraction

Fig. 13. Soot volume fraction statistics for the case with the secondary air injection compared to the experiment.